

Microstructural quantification, modelling and array ultrasonics to improve the inspection of austenitic welds

C Nageswaran, C Carpentier and Y Y Tse

Submitted 20.05.09
Accepted 28.10.09

The fundamental obstacle to characterising accurately the defects in austenitic welds is the distortion of the sound field due to the anisotropic inhomogeneous material. This paper describes the development of the next generation of ultrasonic procedures which use phased array techniques and models to account for the distortion of the sound field, such that the detection, positioning and sizing of defects is improved in comparison to current capabilities.

Each stage of the procedure development is described, along with the issues and obstacles which must be overcome. The electron back-scatter diffraction technique is used to evaluate the texture of the weld and then the microstructural information is input to a model capable of propagating ultrasonic waves through the anisotropic inhomogeneous medium. With knowledge of the distortion, a strategy of adapting the focal laws using time reversal concepts to improve sensitivity was developed.

Keywords: Phased arrays, ultrasonic testing, electron back-scatter diffraction, austenitic welds, time reversal and models.

1. Introduction

The difficulties associated with the ultrasonic non-destructive evaluation of austenitic welds are well known. The fundamental issue is the distortion of a propagating elastic stress wave (*ie* sound) by the coarse-grained anisotropic weld metal. The large grains tend to scatter the sound energy, leading to increased attenuation, and the propagation path is 'skewed' due to the anisotropy of the crystal structure and the differences in texture between different regions in the weld. Consequently, the noise due to grain back-scattering reduces the sensitivity (*ie* signal-to-noise (S/N) performance) and the sound beam skewing leads to incorrect interpretation of flaws – *ie* positioning and sizing errors. Additionally, the weld metal condition can conspire to generate spurious indications which could be erroneously interpreted as defects that threaten structural integrity⁽¹⁾.

Previous efforts have concentrated on the development of advanced probes⁽²⁾ and techniques⁽³⁾ to address the present problem. In recent times, the development and increasing maturity of three fields have opened the possibility of overcoming the difficulties of inspecting austenitic welds, such that the next generation of ultrasonic procedures can inspect the welds in critical components with reduced errors and greater confidence. The three fields are: (1) microstructural quantification, (2) models and (3) array ultrasonic technology.

The ongoing project termed DISSIMILAR (www.dissimilarweld.co.uk) is an attempt to draw together the tools from

Channa Nageswaran and Capucine Carpentier are with TWI Ltd, Granta Park, Great Abington, Cambridge CB21 6AL, UK. Tel: 01223 899 000; Email: channa.nageswaran@twi.co.uk

Yau Yau Tse is with the University of Birmingham, Edgbaston, Birmingham B15 2TT, UK.

within these three fields to generate novel ultrasonic inspection procedures tailored to austenitic welds. This paper presents results to date, illustrating the methods used to quantify the microstructure, modelling results and the strategies being explored to overcome the distortion of the sound field.

2. Approach

2.1 Microstructural quantification

To design the inspection with due consideration to the complex material through which the ultrasound has to propagate, the material must be quantified. In the case of the coarse-grained anisotropic austenitic metals, the description must (1) identify the grain boundaries and (2) evaluate the texture developed in the weld. Furthermore, to evaluate the implications to sound propagation, the elastic stiffness encountered by a wave must be known.

The initial use of the electron back-scatter diffraction (EBSD) technique for the quantification and mapping of austenitic weld microstructure for inspection design was recently presented⁽⁴⁾. The EBSD technique implemented in a scanning electron microscope is widely used to determine the microtexture of crystalline materials⁽⁵⁾.

In the past, researchers have made use of X-ray diffraction analysis to determine the crystalline structure of the weld metal⁽⁶⁾. Analysis showed that the columnar grains solidify along the [100] crystal axis, with the austenite taking the face centered cubic (FCC) unit crystal. Hence the researchers subsequently used macrographs to identify several distinct homogeneous regions where the dendrites had uniform grain orientation⁽⁶⁾.

The crystallographic orientation of the entire weld cross-section at several lengthwise positions was mapped using EBSD. Figure 1 shows a macrograph of a dissimilar weld. The weld was sectioned into seven zones for scanning by EBSD; this paper will make use of the weld structure in zone 1, the weld root.

For scanning the weld map cost effectively through EBSD, the spatial scanning resolution must be established. The scanning resolution impacts on the time taken to generate the map: scan of an area ~4 mm² at a resolution of 5 µm takes ~6 h whereas the same area at a resolution of 40 µm takes only 6 min. The transducer frequency was set at 2 MHz, generating a longitudinal wave with a wavelength of ~3 mm. Assuming the dominant Rayleigh scattering mechanism⁽¹⁾ the wave would be sensitive to a minimum scatterer size of 300 µm, *ie* 1/10 of the wavelength. Hence, a scanning resolution of 40 µm was deemed sufficient to capture significant regions within the weld.

The second important parameter to establish is termed the misorientation angle. The EBSD data is represented as a colour map where each colour corresponds to a particular orientation of the crystal structure with regard to the sample coordinate system. The orientation of the crystals can be expressed in terms of the three Euler angles⁽⁵⁾, which are rotations performed in a specific sequence to transform the sample coordinate system onto the crystal coordinate system. The misorientation parameter is used to define the position of the grain boundaries, *ie* the higher the parameter

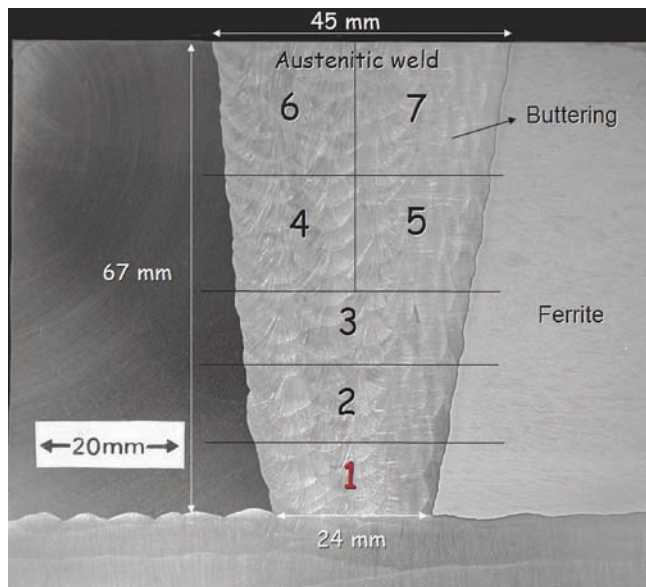


Figure 1. An austenitic weld showing the buttering and cladding layers, and the section zones for EBSD scanning

the smaller the numbers of grain boundaries. Establishment of this parameter is an ongoing activity and is subject to modification due to both experimental validation results and parametric modelling studies of significant orientation mismatches across boundaries. On the first iteration, the misorientation parameter was again set using the Rayleigh scattering assumption, *ie* the misorientation angle is that which leads to the size of the regions in the path of the propagating wave being no less than 300 μm , the minimum scatterer size. An advantage of the misorientation parameter, unlike the scanning resolution, is that any value can be chosen post-scanning, as it is applied on the collected data to generate the maps.

Figure 2 shows the macrograph of zone 1 and the associated EBSD map, where faint black lines within the scan map illustrate general orientation of homogeneous regions. Firstly, note the impact of different deposition procedures for the weld and the buttering, where the buttering was applied prior to flat 1G position manual deposition of the weld. Secondly, the grains appear to grow through several deposit runs leading to the characteristic columnar grain structure observed in austenitic welds.

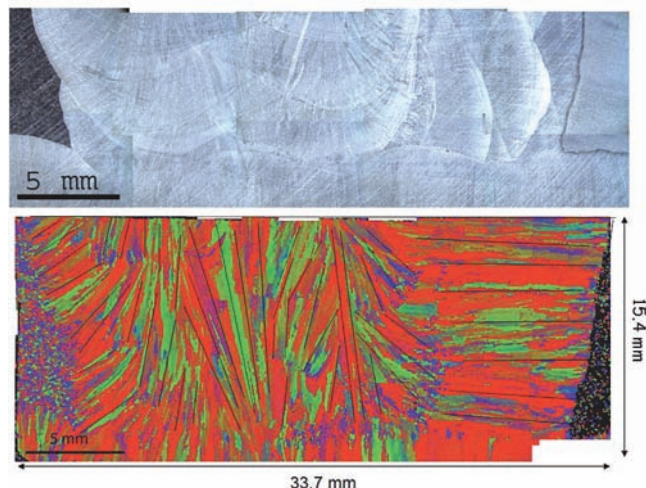


Figure 2. The macrograph of zone 1 and the associated EBSD orientation map; scanned at a resolution of 40 μm and processed with a misorientation parameter of 20°

The weld map, however, had excessive boundaries for cost-effective expression within the model (see section 3.2). Hence, a processing method was devised termed 'orientation unification'. In this technique, several dominant orientations are identified within

the weld map shown in Figure 2. Subsequently, an angular spread of between 15 and 20° either side of the dominant orientation is set to be equal to the dominant orientation; all other regions (and those smaller than the minimum scatterer size) take the nominal orientation of the grain or that of the parent. In addition, the Euler angles (referenced to the axes of the unit cubic cell) are transformed to the rotation angles following the rotation sequence adapted by the simulation program. Figure 3 shows the processed weld map ready for input to the ultrasonic models and Table 1 shows the ten selected dominant orientations for zone 1. The development of the orientation unification technique is ongoing and is subject to feedback from experimental validation trials.

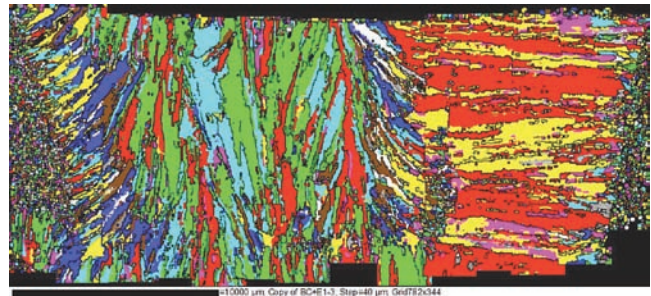


Figure 3. Processed weld map for input to the models; the ten dominant orientation regions are detailed in Table 1

Table 1. The ten dominant orientations selected for the weld map of zone 1; the crystallographic orientations are expressed as three rotation angles about the x, y and z axes of the component reference frame, as required for ultrasonic modelling

Colour	$\alpha(^{\circ})$ (rotation about x)	$\beta(^{\circ})$ (rotation about y)	$\gamma(^{\circ})$ (rotation about z)
Red	0	0	0
Blue	0	0	45
Lime green	318.72	6.37	193.09
Yellow	12.55	28.25	18.91
Cyan	8.17	4.52	338.91
Brown	30.81	-13.14	29.96
Pink	348.11	-22.77	177.97
Green	21.73	-1.78	8.36
White	351.5	-22.86	138.12
Black	19.95	-1.16	56.60

The elastic stiffness of the various mapped regions of the weld has to be determined to model the propagation of a stress (*ie* sound) wave. In a previously reported approach⁽⁶⁾, a thin sample from a region of the weld containing columnar grains oriented in the same direction was removed. The stiffness was then evaluated using through-transmission experimental measurement of ultrasonic velocities. The weld was then discretised into regions where the grains had similar orientations, the assumption being that the solidification direction along the [100] axis is in the orthogonal plane to the welding direction, and that all the homogenised regions of the weld contain similar columnar grains such that the weld can be described using just the angle of the columnar grain orientation⁽⁶⁾.

Figure 3 shows that the weld and buttering consist of grains of differing crystallographic make-up, hence the EBSD map offers the possibility to describe the weld in its full three-dimensional state. The stiffness is evaluated using a single crystal of the weld alloy grown through a casting process. The velocity of the longitudinal and the two polarised shear waves along [100], [110] or the [111] are related, by Newton's Law of Motion and Christoffel's equation, to the stiffness of the cubic crystal. The results presented in this paper make use of the cubic stiffness constants measured on an

alloy of similar composition to the weld presented in Figure 1 using velocity measurements in a single crystal⁽⁷⁾. The measured stiffness constants are $C_{11}=203.6$ GPa, $C_{12}=133.5$ GPa and $C_{44}=129.8$ GPa.

2.2 Modelling

The CIVA⁽⁸⁾ model is being used as the primary platform to develop, test and optimise the strategies to overcome the distortion of the austenitic weld⁽⁴⁾. The semi-analytical codes to model ultrasonic wave propagation and interactions with discontinuities in anisotropic media are cost effective for industrial parametric studies, in comparison to finite element/difference codes which are computational and time intensive.

A recent example of the current capabilities of CIVA to deal with anisotropic media was illustrated through the ultrasonic inspection of a 69 mm-thick K-prep 316L austenitic weld⁽⁹⁾. The inspection of the weld with a 2 MHz single-element transducer generating a 60° longitudinal wave was both simulated and experimentally evaluated on a mock-up specimen. The distortion of the propagating sound beam was simulated by the CIVA model and compared to experimental results⁽⁹⁾. In general, the experimental evidence was consistent with the model predictions; however, there were discrepancies in signal amplitudes and echo-dynamics. This shows the importance of describing the weld structure accurately, as well as the need for validation of the model. The authors conclude with the importance of taking into account the distortion to better design inspections and improve sizing of defects⁽⁹⁾.

The weld map of Figure 3 was processed using a digitiser to generate a 2D CAD drawing⁽⁴⁾. The boundaries were manually identified according to the criteria of minimum scattering regions/distances. Figure 4 shows the expression of the zone 1 weld cross-section within the CIVA model, containing 89 closed regions leading to a total of 1276 boundaries. The weld cross-section is extruded to create the three-dimensional component, *ie* assumes that the weld structure is uniform along the welding direction.



Figure 4. The CAD drawing of the zone 1 weld cross-section input into the CIVA model. The drawing consists of 89 closed regions with a total of 1276 boundaries

The CIVA model is used here to illustrate the distortion induced by the microstructure onto the sound field. In all the results presented in this paper, a 2 MHz linear phased array probe with a pitch of 1.5 mm is used in the inspection simulations. Figure 5(a) shows the ray trace of a 16-element array generating a 45° longitudinal wave beam (green trace) and associated shear beam (red trace) within zone 1 of the weld, when all the regions in the weld take the stiffness value of the parent austenitic, *ie* the weld is isotropic. Note that the array is not programmed to focus the sound field, only steer. Figure 5(b) shows the ray tracing of the sound beams when the full anisotropic weld structure is input, *ie* each region takes the set dominant orientations. The distortion due to the microstructure is illustrated by the ray tracings which are no longer straight; note that the red shear wave of Figure 5(a) becomes two orthogonally polarised shear wave components in the three-dimensional anisotropy of the weld in Figure 5(b).

The bars above the array associated with each element represent the delay applied to each element. The delay law applied for the isotropic weld in Figure 5(a) dictates that the first element fires first followed by successive firing of the adjacent element up to element

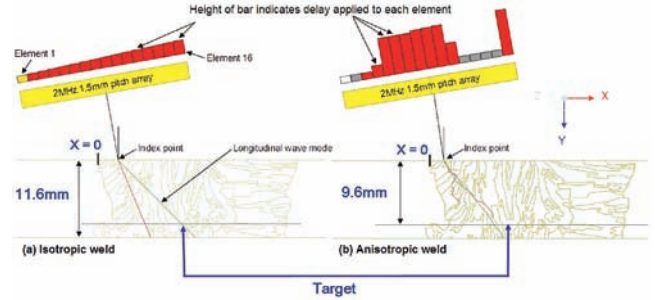


Figure 5. Ray tracing of a 2 MHz 16-element array with a pitch of 1.5 mm programmed to generate a 45° beam within (a) an isotropic weld and (b) an anisotropic weld measured by EBSD. The array was inclined at 10° to the horizontal and is in immersion with a water path of 10 mm

number 16. Hence, the delay of elements 2 to 16 are relative to element 1, which fires at time equals zero. In Figure 5(b) the CIVA model has used the criteria of generating a longitudinal beam at 45° to set the delay law such that only those elements which contribute to the goal are activated, *ie* elements 1, 2, 12, 13, 14 and 15 are turned off. Note, however, the microstructural condition does not appear to allow optimisation of the delay law such that the longitudinal ray trace passes through the same target point as in the isotropic medium.

The beam sections in the x-z plane 9.6 mm from the surface (see Figure 5) are evaluated using the CIVA model; Figure 6 shows the results of the three cases which were considered. Note that the index point of the sound incident on the surface of the component was at $x = 3$ mm (see Figure 5). Figure 6(a) presents the beam of the case shown in Figure 5(a), *ie* the weld is isotropic and the beam is generated using the isotropic delay law, and the beam profile is as expected. Figure 6(b) represents the case shown in Figure 5(b), *ie* with the anisotropic weld properties included and the delay law calculated by CIVA to propagate the beam. The distortion due to the microstructure is revealed by the output and the maximum amplitude of the beam in Figure 6(b) is 27 dB less than the isotropic case shown in Figure 6(a).

A further case was considered, shown in Figure 6(c), where the isotropic delay law shown in Figure 5(a) was used to generate the sound and propagate it within the anisotropic weld. The loss in signal amplitude in the case shown in Figure 6(c) was only 19 dB less than the isotropic case. Hence, turning off elements in the array when generating the delay law (*ie* the anisotropic delay law generated by CIVA for the case shown in Figure 6(b)) reduces the amount of energy coupled into the weld, which would in turn impact on the S/N performance of the inspection.

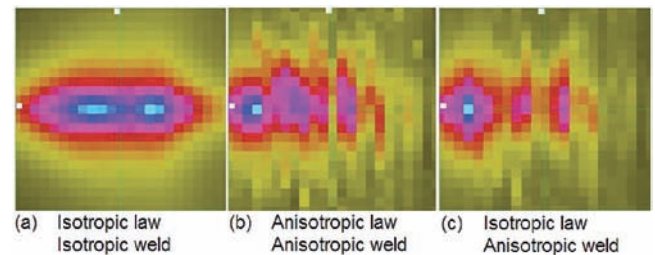


Figure 6. Beam sections calculated in the x-z plane at a depth of 9.6 mm from surface for (a) isotropic delay law for an isotropic weld, (b) anisotropic delay law calculated by CIVA for an anisotropic weld and (c) the isotropic delay law applied for an anisotropic weld

A simulation of using the 2 MHz 16-element probe to scan the weld along a line from $x = -5$ mm to $x = 9$ mm with a resolution of 1 mm was performed. A 3 mm-diameter side-drilled hole (SDH) target was introduced at a depth of 9.6 mm, *ie* where the beam sections of Figure 6 were evaluated. Figure 7 shows the results of the simulated scan.

In the isotropic case of Figure 7, the 45° beam is directly incident on the SDH at an index position of $x = 3$ mm, giving the largest signal amplitude. However, in the anisotropic case, the maximum signal amplitude was received at an index position of $x = 9$ mm, which is 19 dB below the signal received from the target SDH in the isotropic case (see Figure 7). In fact, at $x = 3$ mm in the anisotropic case shown in Figure 7, the signal strength was 13.6 dB weaker than at $x = 9$ mm in the same case. Note that the model only resolves the interaction of the sound field with the SDH target, *ie* no boundary interactions are evaluated, such that no back-scattered noise signals are predicted.

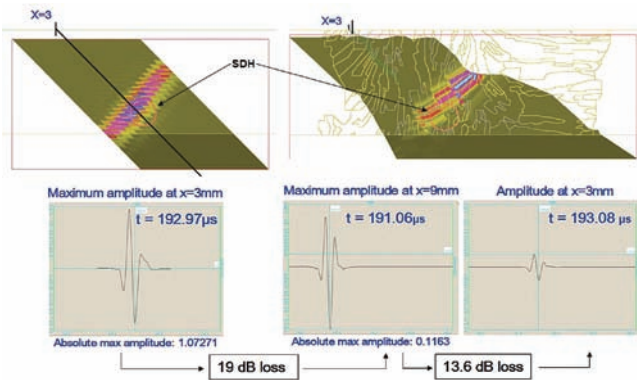


Figure 7. A simulated scan in CIVA from an index point of $x = -5$ mm to $x = 9$ mm. A 3 mm SDH was introduced at a depth of 9.6 mm from the surface in an isotropic medium (left) and in the anisotropic weld (right)

In summary, the observed errors in plotting signals from flaws due to the distortion of the sound field by the microstructure of austenitic welds is predicted by the CIVA simulation platform. In the ongoing project, the predictions of the CIVA model are being validated with experimental data and the effectiveness of the EBSD route to quantify the microstructure will be assessed. The main aim of the project, however, is the development of strategies to overcome the distortion induced by the microstructure.

3. Strategies

3.1 Adapted focal laws to maximise sensitivity

As noted in Figure 6, reducing the number of elements used on an array directly impacts on the energy coupled into the weld, subsequently reducing the sensitivity of the inspection. Hence, the delay law should aim to make use of all available elements on the array. The anisotropic microstructure of the weld induces different travel paths to waves emanating from different positions on the surface. This is illustrated by the simulated arrival times of the signals due to the SDH in Figure 7. In the isotropic case (shown on the left of Figure 7) the arrival time of the peak signal due to the SDH was $192.97 \mu\text{s}$ at a probe index position of $x = 3$ mm, whereas within the anisotropic weld (shown on the right) at a probe position of $x = 3$ mm the signal was received at $193.08 \mu\text{s}$, $0.11 \mu\text{s}$ later. This implies that the actual travel path to the SDH target in the anisotropic weld is longer than a straight line path.

The proposed strategy to improve sensitivity makes use of all available elements on the array and time reversal concepts to generate focal laws ‘adapted’ to the anisotropic condition of the weld⁽⁴⁾. The widely divergent sound field generated by each element on the array will be distorted by the microstructure but some of the energy will be incident on the target area. The fundamental theory underlying the algorithms of focal law calculators to focus the sound energy from an array is to ensure that the wave fronts from each element arrive at the target position at the same time (assuming velocity is constant) and in the correct phase to constructively generate a maximum in sound pressure. The adapted

focal laws will be generated by using simulations to predict the actual time at which the sound energy from all the elements arrives at the required target region.

This time reversal concept executed on the simulation platform does not require the introduction of SDHs in the actual structure to be inspected in order to generate a better adapted focal law. However, if sufficient S/N performance could be achieved from each element of the actual array, the received echoes from a defect could be used to implement the time reversal concept online during inspection. To enable this experimental approach to complement the simulation, advanced materials and manufacturing techniques are being developed to achieve sufficient S/N from each element of the array.

Similarly, for application in industry, the proposed method does not require the detection of the flaw to implement an adapted delay law to image it clearly. On the first iteration, the array controller will be programmed with a matrix of position-dependent adapted laws (which were generated within the simulation). The inspection will be performed with the intention that the focal laws are better adapted for the region they are inspecting. On the second iteration (assuming sufficient S/N performance from each element could be achieved), an experimental implementation of the time reversal concept could be explored using any detected echoes – *ie* an online feedback routine to generate an experimentally adapted focal law – to image it further.

This simulated time reversal concept for generating adapted focal laws is illustrated using zone 1 of the weld (shown in Figure 1), its anisotropy quantified by EBSD (see Figure 3) and expressed within the CIVA simulation platform. A 2 MHz linear array with eight elements at a pitch of 1.5 mm is coupled to the model description of zone 1 of the weld in immersion testing. The probe was inclined at an angle of 10° to the horizontal and the index point of the probe was set to $x = 2$ mm (see Figure 8). In the first case, a water path length of 140 mm is selected to place the SDH target very close to the range of the natural near-field point (end of the Fresnel zone) of the array.

The simulation shown in Figure 8 is used to first illustrate that the concept of generating the delay law through received signals from the target SDH (*ie* the adapted law) is sound since, at the near-field range, its performance should be similar to that of the calculated law. Secondly, the simulation is used to study the sensitivity of the received signal amplitude in two different scenarios: (1) the null-point of the wave, where the arrival phase of all waves is at zero amplitude, was chosen as the reference to generate the adapted delay law, and (2) the adapted law generated was reversed without taking into account the pulse-echo nature of the travel time. Both these scenarios illustrate the degree of S/N performance change that could take place due to the nature of the delay law used when

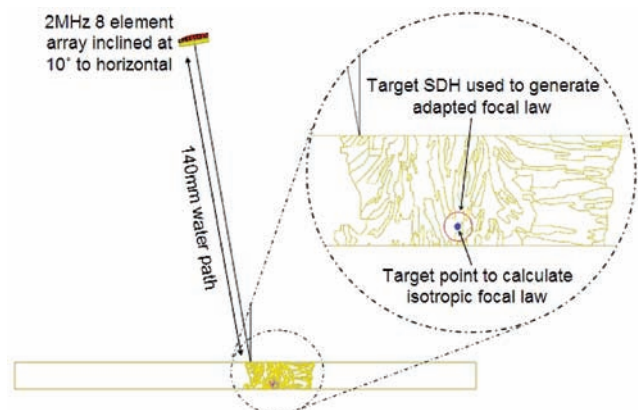


Figure 8. Simulation of the anisotropic weld inspection with a 2 MHz linear array of eight elements at a pitch of 1.5 mm, inclined at 10° to the horizontal with a water path of 140 mm; the index point of the probe was set to $x = 2$ mm

inspecting an anisotropic weld, as well as the precision available in the simulation platform.

The isotropic delay law was calculated by ensuring that the sound energy from all eight elements arrives at the target point (see Figure 8) at the same time and in phase to constructively interfere for maximum sound pressure; the algorithm used was termed ‘single point focusing’ in the CIVA model. The adapted focal laws were not calculated mathematically. Each element of the array was fired and received on within the simulation, recording the reflected signal from the target SDH shown in Figure 8, while all other elements were turned off. Each element, due to its small size, would generate a widely divergent beam and the model evaluates the interaction of this beam front with the SDH after traversing the anisotropic weld. Due to the distortion induced by the microstructure, sound energy emanating from different points (*ie* elements) on the array will take different paths to the SDH. This is shown in the A-scan signals from the SDH due to the eight elements where the arrival times are offset with respect to each other, as shown in Figure 9, and the non-uniformity of the offsets suggests that it is induced by a phenomenon in addition to the difference in the geometrical direct line paths to the target SDH. Figure 9 also shows the difference in received signal amplitude with respect to that of element 1, illustrating the degree to which the microstructure influences the propagation of sound energy within the weld. The amplitude results imply that each element will impart differing amounts of sound pressure to the composite wave front generated at the target region, hence some elements are more influential than others towards generating high sound pressure amplitudes for any given microstructural path.

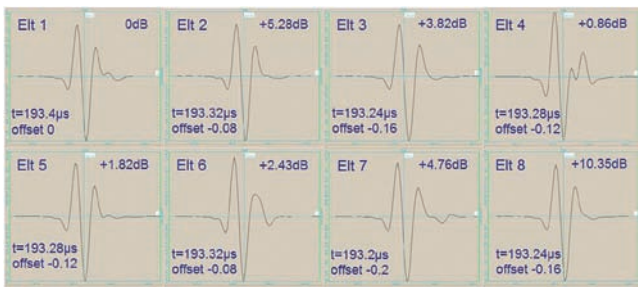


Figure 9. A-scans from each of the eight elements collected independently of all others. The arrival times are shown, with their offset from element 1, along with the change in received amplitude relative to element 1

The simulated arrival times to the target are used to generate the adapted focal law, following the same criteria as for the calculated focal law (assuming an isotropic weld): the wave fronts must arrive at the target at the same time and in phase to maximise the sound energy. The isotropic and adapted focal laws applied to the eight-element array are illustrated in Figures 10(a) and 10(b), respectively, along with the resultant echo signal from the SDH target. In addition, the results from the two scenarios described earlier are shown in Figure 10(c) and 10(d).

The adapted law (Figure 10(b)) showed similar performance to

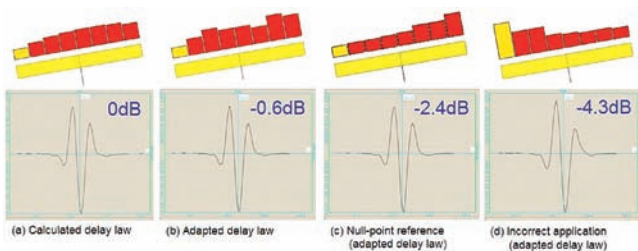


Figure 10. Illustration of (a) calculated focal law assuming isotropic conditions, (b) adapted focal laws generated through simulation, (c) adapted focal law generation using the null-point of the received signal as reference and (d) incorrect adapted delay law, applied in reverse to the array without accounting for pulse-echo travel path

the calculated law (less than 1 dB) at the near-field range, which is at the edge of the range at which the delay laws begin to impact on the S/N performance. The sensitivity of the received signal to changes in the applied delay laws of less than 0.1 μ s (shown in Figures 10(c) and 10(d)) illustrate the level of change in S/N performance that could be observed even at the edge of the applicable envelope (*ie* the near-field range).

In the second case, the water path length shown in Figure 8 is now reduced to 10 mm, while all other simulation parameters such as number of elements, incident point and so on were kept as for case 1. The array is now at a range smaller than the near-field range where focusing algorithms can have significant influence on the sound field characteristics. Table 2 shows the calculated and time reversed adapted delays applied to the eight elements in both transmission and reception. Additionally, the signal amplitudes and arrival times of the echoes generated by the SDH target in the anisotropic weld for each of the elements is presented.

Table 2. The calculated and adapted delays applied to the eight elements of the array (in transmission and reception). The arrival times of the echoes generated by the SDH target within the anisotropic weld and their amplitudes (both the absolute output by the model and relative to element 1) are also presented

Element	Calculated delay law (μ s)		Corrected delay law (μ s)		Arrival time (μ s)	Absolute amplitude	Relative amplitude (dB)
	T	R	T	R			
1	0.000	0.095	0.020	0.120	17.88	2.44E-03	0.0
2	0.040	0.055	0.000	0.140	17.92	4.81E-04	-14.1
3	0.070	0.025	0.040	0.100	17.84	6.28E-04	-11.8
4	0.090	0.005	0.080	0.060	17.76	5.60E-04	-12.8
5	0.095	0.000	0.140	0.000	17.64	1.67E-03	-3.3
6	0.090	0.005	0.140	0.000	17.64	4.95E-03	6.1
7	0.070	0.025	0.140	0.000	17.64	1.47E-02	15.6
8	0.025	0.070	0.130	0.010	17.66	2.00E-02	18.3

Figure 11 shows the received signal from the SDH when using the calculated and adapted delay laws, where the amplitude of the received signal using the adapted delay law was 1.7 dB greater than when using the calculated delay law. The case presented here was at a single incident position and a specific microstructural condition but the concept of adapting the focal laws to the microstructure of the weld could potentially lead to significant improvement in S/N performance.

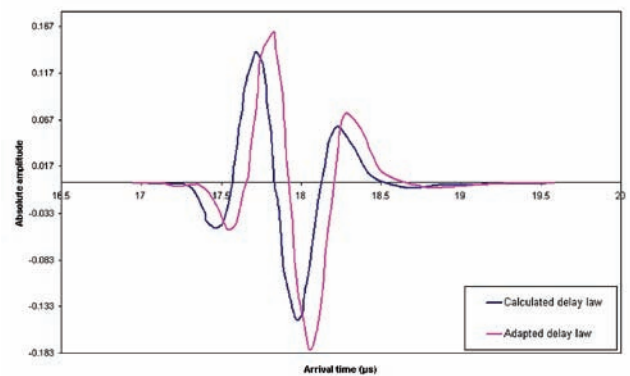


Figure 11. Received signals from the target when using the calculated and adapted delay laws; the signals are offset in time with the signal due to the adapted law being 1.7 dB higher

Figure 12 shows a further case with an 85 mm-thick austenitic weld which contains a rectangular flaw near the root, above the buttering. Figure 12(a) shows the full EBSD scan of the weld and Figure 12(b) shows the processing of the weld into the model along with the inspection scenario. Note that only the ‘relevant’ part of the weld is used in the model, *ie* the material through which the sound will propagate to the flaw; by not evaluating the sound propagation over the full description of the weld the computing times can be reduced significantly.

The inspection was simulated using a 32-element linear array on a Perspex wedge optimised for generating longitudinal waves. The calculated delay law was designed to focus the sound at the depth of the flaw assuming that the weld is isotropic; the adapted

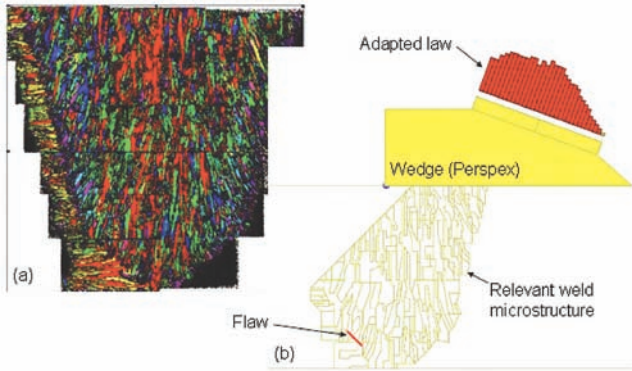


Figure 12. The inspection scenario on an 85 mm-thick austenitic weld, showing the adapted delay law generated for a 32-element linear array on a Perspex wedge designed to generate longitudinal waves: (a) shows the full weld map using EBSD and (b) shows the relevant part of the weld processed into the model

delay law was generated as described above. In the simulation, the probe and wedge were moved a distance of 14 mm (with 1 mm resolution) on the surface such that the beams traversed the area of the flaw. The resultant B-scan due to the simulated scanning is presented for three distinct cases in Figures 13, 14 and 15.

Figure 13(a) illustrates the case where the weld was absent, *ie* the medium was isotropic, taking nominal value for the longitudinal wave velocity in stainless steel (5750 m/s). The delay law was calculated to focus the sound energy to the centre of the flaw and, as shown in Figure 13(b), the maximum signal was plotted near the flaw centre. The simulated time of flight for the maximum signal on the flaw centre was 46.26 μ s (Figure 13(c)).

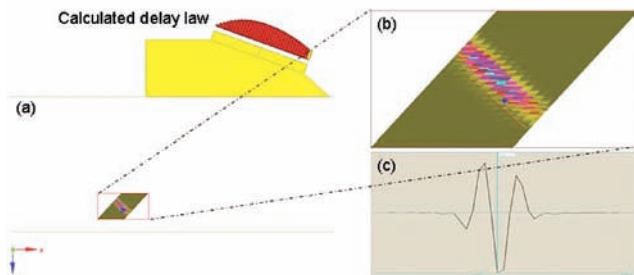


Figure 13. The inspection scenario where the anisotropic weld was absent: (a) shows the case with the calculated delay law, (b) shows the plotted signal and (c) shows the A-scan at flaw centre

Figure 14(a) illustrates the case where the anisotropic weld description was introduced. The delay law was again the same calculated one used in the case of Figure 13. This case represents what is presently proposed in procedures for inspection of austenitic welds, where the weld condition is not taken into account when the inspection is designed. Figure 14(b) illustrates the resultant

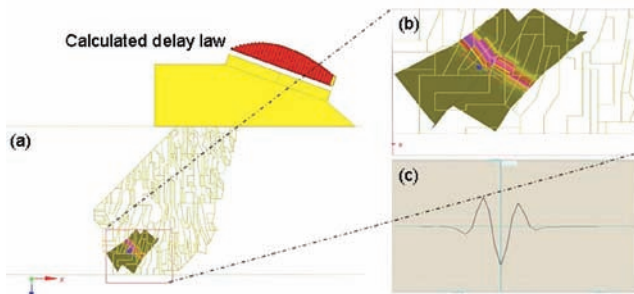


Figure 14. The inspection scenario where the anisotropic weld is introduced but the delay law calculation assumed an isotropic medium: (a) shows the case with the calculated delay law, (b) shows the plotted signal with the induced positioning error and (c) shows the A-scan at flaw centre

errors induced in plotting, where the maximum echo signal plots >6 mm away from flaw centre, with the A-scan signal over the flaw 4.5 dB less than at the maximum (Figure 14(c)). The simulated time of arrival of the signal on flaw centre was 44.59 μ s (Figure 14(c)).

Figure 15(a) illustrates the case with the anisotropic weld introduced and where the adapted delay law was generated using the time reversal concept for each element of the array. Figure 15(b) shows the simulated results where the signal maximum plots <1 mm from flaw centre and the signal strength is nearly 2 dB higher in comparison to the maximum signal strength of the case shown in Figure 14. The simulated time of arrival of the signal on flaw centre was 45.43 μ s (Figure 15(c)), which is 0.84 μ s later than in the case of Figure 14, illustrating the degree of distortion imparted by the weld medium. Clearly, the simulation results then illustrate the degree to which positioning errors can be reduced, in addition to gains in S/N, when the delay law is appropriately adapted for the medium.

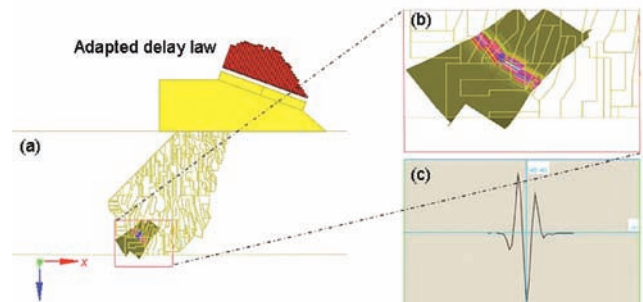


Figure 15. The inspection scenario where the anisotropic weld is introduced and the adapted delay law was used instead of the calculated one: (a) shows the case with the adapted delay law, (b) shows the plotted signal with positioning error <1 mm and (c) shows the A-scan at flaw centre

The use of finite element codes modelling the full EBSD weld map at a resolution of 40 μ m is also being investigated for generating the adapted focal laws, *ie* as an 'adapted delay law calculator for anisotropic media'. Finite element codes currently take excessive computing resources and time to simulate full ultrasonic inspections, which can be done more cost effectively, in relative terms, by the semi-analytical codes employed in the CIVA simulation platform. However, greater precision in the delay law curves could be achieved through the use of the finite element codes which model the full anisotropy of the weld without simplifications, *ie* splitting the weld map into regions of dominant orientation for input into the CIVA model.

3.2 Issues

The EBSD technique is only being used to evaluate the crystalline orientation of the weld on the transverse plane to the welding direction. A non-destructive experimental method was devised to evaluate the microstructural uniformity of the weld along the welding direction. In addition, full EBSD maps of the weld at several positions along it are being generated to quantify the degree to which the microstructure changes along the welding direction.

As stated earlier, the scanning resolution for generating the EBSD maps determines how long each scan takes. At the 40 μ m resolution used for the scan of zone 1 shown in Figure 1, the total time for scanning alone is estimated at about 10 h, excluding the considerable amount of time for sample preparation. To prepare, scan and process several full weld cross-sections, the total time is measured in weeks. Hence, this method is costly and is only likely applicable for critical welds, where the consequences of failure would be economically, environmentally and socially catastrophic. Future developments in EBSD technology could lead to a reduction in the times taken to generate the weld maps, opening the possibility of application to a wider set of components.

Similar to EBSD scanning, the time taken to simulate a single case with an anisotropic weld in comparison to an isotropic case on the CIVA platform is considerable. For example, the time taken to run the case in the isotropic weld shown in Figure 6(a) was 1 min, whereas it took 7.5 h to compute each of the other two cases in the anisotropic weld. Similarly, the isotropic case shown in Figure 7 was completed in four minutes while the anisotropic case took in excess of 100 h.

Clearly, this has implications towards the applicability of the proposed correction strategies as large weld maps need to be modelled, as well as more complex probe designs with up to 128 elements. A proposed simplification is to model the anisotropy in the path of the propagating wave, while assigning isotropic properties to the remaining regions of the weld. Modelling times could be reduced by coding faster numerical stencils or modifying parameters. The most practical route available presently is to increase as much as possible the computing resources available to run the model.

Empirical modelling studies of the significant orientation changes across a boundary (*ie* grain boundary) were undertaken in order to identify and limit the number of different dominant orientation regions. Similarly, investigations into the effect of compositional variation on the elastic stiffness of alloy single-crystals in comparison to the stiffness of the dominant element were established to accurately model propagation.

An important aspect of the work has to be validation, as noted by other researchers in the field⁽⁹⁾. The use of models, especially for critical applications, has to be subject to stringent evidence, not only to qualify their applicability but, more importantly, to establish the limits to their validity.

4. Conclusions

The following conclusions are drawn from the work done to date in the ongoing DISSIMILAR project:

- The evidence to date shows that the application of the strategy to better design the focal laws by taking into account the anisotropic microstructure has potential to improve inspection quality. In the project, this strategy is being tested and validated using a specimen with implanted flaws.
- A technique termed *orientation unification* has been devised to translate the orientation map generated by EBSD into the ultrasonic simulation platform. The technique is being refined and optimised to set the dominant orientations in order to reduce the number of regions required to describe the weld.
- The methods being explored are only applicable to welds in critical components (such as the safe-end weld in a reactor pressure vessel) due to the cost, complexity and time required for implementation.

Acknowledgements

The authors would like to thank all members of the DISSIMILAR consortium (British Energy, Shell UK, HSE Nuclear Installations Inspectorate, Peak NDT, ALBA Ultrasound, Applied Inspection, Birmingham University and TWI) for their support and encouragement. In addition, the authors are grateful for the support and encouragement of Colin Bird throughout the project to date.

The DISSIMILAR project is part funded by the United Kingdom's Technology Strategy Board.

References and footnote

1. J Krautkrämer and H Krautkrämer, 'Ultrasonic testing of materials', New York, Springer-Verlag, 1990.
2. C Nageswaran, C R Bird and A C Whittle, 'Immersion transmit-receive longitudinal phased array probe for stainless steel', *Insight*, Vol 50, No 12, pp 673-684, December 2008.
3. C Nageswaran and C R Bird, 'Evaluation of the phased array

transmit-receive longitudinal and time-of-flight diffraction techniques for inspection of a dissimilar weld', *Insight*, Vol 50, No 12, pp 678-684, December 2008.

4. C Nageswaran, C Carpentier and Y Y Tse, 'Improving phased array ultrasonic testing using models to overcome austenitic weld distortion', *Proc 7th Int Conf on NDE in Relation to Structural Integrity for Nuclear and Pressurised Components*, Yokohama, May 2009.
5. V Randle, 'Microtexture determination and its applications', London, Institute of Materials, 1992.
6. O Dupond, B Chassignole, L Doudet and C Birac, 'Methodology for modelling ultrasonic inspection of an austenitic stainless steel weld', *Proc 6th Int Conf on NDE in Relation to Structural Integrity for Nuclear and Pressurised Components*, Budapest, October 2007.
7. J Lenkkeri and A Juva, 'The effect of anisotropy on the propagation of ultrasonic waves in austenitic stainless steel', *Reliability of Ultrasonic Inspection of Austenitic Materials*, Belgium, 1980.
8. P Calmon, S Mahaut, S Chatillon and R Raillon, 'CIVA: An expertise platform for simulation and processing NDT data', *Ultrasonics*, Vol 44, pp 975-979, 2006.
9. B Chassignole, O Paris and E Abittan, 'Ultrasonic examination of a CVCS weld', *Proc 6th Int Conf on NDE in Relation to Structural Integrity for Nuclear and Pressurised Components*, Budapest, October 2007.

Copyright © 2009, TWI Ltd.